Quantitative intravital calcium imaging maps single cellbehavior to kidney tubular structure

Martins, Joana Raquel ; Haenni, Dominik ; Bugarski, Milica ; Figurek, Andreja ; Hall, Andrew M

Abstract: Ca2+ is an important second messenger that translates extracellular stimuli into intracellular responses. Although there has been significant progress in understanding Ca2+ dynamics in organs such as the brain, the nature of Ca2+ signals in the kidney is still poorly understood. Here, we show that by using a genetically expressed highly sensitive reporter (GCaMP6s), it is possible to perform imaging of Ca2+ signals at high resolution in the mouse kidney in vivo. Moreover, by applying machine learning-based automated analysis using a Ca2+-independent signal, quantitative data can be extracted in an unbiased manner. By projecting the resulting data onto the structure of the kidney, we show that different tubular segments display highly distinct spatiotemporal patterns of Ca2+ signals. Furthermore, we provide evidence that Ca2+ activity in the proximal tubule decreases with increasing distance from the glomerulus. Finally, we demonstrate that substantial changes in intracellular Ca2+ can be detected in proximal tubules in a cisplatin model of acute kidney injury, which can be linked to alterations in cell structure and transport function. In summary, we describe a powerful new tool to investigate how single cell behavior is integrated with whole organ structure and function and how it is altered in disease states relevant to humans.

DOI: https://doi.org/10.1152/ajprenal.00052.2020

Quantitative intravital calcium imaging maps single cell behavior to kidney tubular structure

Martins JR[1], Haenni D[1,2], Bugarski M[1], Figurek A[1], Hall AM[1,3].

[1]Institute of Anatomy, University of Zurich, Switzerland. [2]Center for Microscopy and Image Analysis, University of Zurich, Switzerland. [3]Department of Nephrology, University Hospital Zurich, Switzerland.

Address for correspondence:

Andrew Hall PhD MRCP (UK)
Institute of Anatomy
University of Zurich
Winterthurerstrasse 190
8057 Zurich
Switzerland
Email: andrew.hall@uzh.ch
Tel: +41 (0)44 635 52 25
Fax: +41 (0)44 635 57 02

Word count (excluding references and figure legends): 4032.

Running title: Calcium signaling in the kidney.

Supplementary Materials available at https://figshare.com/s/537b33e39b507142e525 (DOI 10.6084/m9.figshare.11791188)

Keywords: Calcium signaling, intravital microscopy, kidney tubule.

Abstract

Ca^{2+} is an important second messenger that translates extracellular stimuli into intracellular responses. Although there has been significant progress in understanding Ca^{2+} dynamics in organs such as the brain, the nature of Ca^{2+} signals in the kidney is still poorly understood. Here, we show that by using a genetically expressed highly sensitive reporter (GCaMP6s) it is possible to perform imaging of Ca^{2+} signals at high resolution in the mouse kidney *in vivo*. Moreover, by applying machine learning based automated analysis using a Ca^{2+}-independent signal, quantitative data can be extracted in an unbiased manner. By projecting the resulting data onto the structure of the kidney, we show that different tubular segments display highly distinct spatio-temporal patterns of Ca^{2+} signals. Furthermore, we provide evidence that Ca^{2+} activity in the proximal tubule (PT) decreases with increasing distance from the glomerulus. Finally, we demonstrate that substantial changes in intracellular Ca^{2+} can be detected in PTs in a cisplatin model of AKI, and linked to alterations in cell structure and transport function. In summary, we describe a powerful new tool to investigate how single cell behavior is integrated with whole organ structure and function, and how it is altered in disease states relevant to humans.

Introduction

Individual renal tubular epithelial cells have to adjust solute transport in response to changes in demand to maintain whole organ function and overall body homeostasis. Ca^{2+} is an important second messenger that translates extracellular stimuli into intracellular responses (30). Ca^{2+} signals are encoded by amplitude, duration, rate and spatial location, and regulate a variety of important cellular processes (4, 30). Previous *in vitro* experiments have suggested that intracellular Ca^{2+} might be involved in mediating increases in solute transport in the proximal tubule (PT) in response to increases in apical flow (11, 34). Moreover, angiotensin II (36) and α_1 adrenergic sympathetic nerves (17) – which are both thought to induce Ca^{2+} release within cells - increase solute transport in the PT *in vivo*. Meanwhile, Ca^{2+} signaling has also been implicated in flow sensing in the thick ascending limb (19), juxtaglomerular signaling (21), regulation of NCC expression in the distal convoluted tubule (DCT) (13), and activation of flow-induced changes in K^+ secretion in the collecting duct (27, 40). Thus, intracellular Ca^{2+} could play a vital role in regulating solute transport along the kidney tubule (5). Moreover, disordered Ca^{2+} signaling has been postulated to be central to the pathogenesis of cellular damage in acute kidney injury (AKI) following insults such as ischemia and toxins (10).

Intravital multiphoton microscopy of represents a powerful tool to study cellular function *in vivo* (31). However, loading of Ca^{2+} sensitive dyes in the kidney is technically very challenging (20). Genetic expression of sensors provides a more promising approach, and has been used previously to study Ca^{2+} activity in both glomerular and tubular epithelial cells (3, 7, 35, 41). It has been reported that PTs display spontaneous slow Ca^{2+} transients (32, 41), but the exact nature of these and their relationship to kidney architecture was unknown. In addition, it is not clear how they compare to Ca^{2+} signals in other tubular segments. A particular limitation in the field was the sensitivity of older probes to detect physiological

changes in cytosolic Ca^{2+}. Moreover, the relatively high laser powers required precluded repetitive imaging over prolonged periods of time to monitor slowly evolving processes. Thus, there is a need for new technical advances to build a more comprehensive understanding of Ca^{2+} signaling in the kidney.

We have created a new transgenic mouse line expressing a highly sensitive Ca^{2+} reporter (GCaMP6s) in all kidney epithelial cells. Here, we show that intravital multiphoton imaging of these animals in combination with structural markers can be used to elucidate spatial patterns of Ca^{2+} from intracellular to the whole organ level. Moreover, by stabilizing the tissue with a custom-designed stage, continuous imaging of large fields of view can be performed for time periods sufficient for quantitative assessment of Ca^{2+} activity, and without inducing detectable toxicity. In addition, by applying state of the art computational analysis, data can be extracted in an unbiased manner to construct kinetic maps of signal behavior. Using this approach, we show that substantial differences in Ca^{2+} signaling exist between specialized tubular segments. Furthermore, we have found that the majority of spontaneous Ca^{2+} transients in the PT arise in the apical region of cells and propagate basolaterally, and that the frequency of these events decreases with increasing distance from the glomerulus. Finally, we were able to detect substantial changes in Ca^{2+} signaling in PTs in a cisplatin model of AKI, and link these to alterations in cell structure and transport function.

In summary, by leveraging important technological breakthroughs, we describe in detail the landscape of Ca^{2+} signaling in cortical kidney tubules *in vivo*, and how single cell behavior maps to organ architecture.

Methods

Animals

GCaMP6s mice were generated by breeding Ai96(RCL-GCaMP6s) (JAX stock #024106) with CMV-Cre mice (39) (JAX stock #006054). Experiments were performed on 6 to 18 week old male GCaMP6s^{+}/CMV-Cre^{+} (GCaMP6s) mice, in accordance with the regulations of the Zurich cantonal veterinary office (Ref: ZH194/16). GCaMP6s^{+}Cre^{+} mice are viable and fertile with no gross physical or behavioral abnormalities.

Intravital imaging

Animals were anesthetized with an intra-peritoneal injection of ketamine (100 mg/kg) and xylazine (10 mg/kg) and the left kidney was externalized as described previously (38). The internal jugular vein was cannulated allowing intravenous delivery of reagents. Animals were placed on a custom-built temperature-controlled microscope stage and body temperature was monitored throughout experiments. Imaging was performed using a custom-built multiphoton microscope operating in an inverted configuration (28) and powered by a broadband tunable laser (680-1300 nm) (InSight Deep See Dual, Spectra Physics, Santa Clara, CA, USA), with a XLPlan N ×25/1.05 water immersion objective (Olympus, Tokyo, Japan). Emitted light was filtered by the following bandpass filters: 405/150, 525/50, 605/50, 700/75 (AHF Analysentechnik AG). Emission was collected by four highly sensitive gallium-arsenide-phosphide photomultiplier tubes (Hamamatsu, Japan) in a non-descanned epifluorescence detection mode. Images were processed using FIJI image analysis software and its plugins (37) and fluorescence changes over time analyzed using Mathematica.

Dye loading, reagents and imaging parameters

Unless stated otherwise, dyes were purchased from Invitrogen Molecular Probes and all other reagents from Sigma Aldrich (St. Louis, Missouri, USA). Hoechst 33342 (8 mg/kg body

111 weight [bw]) was bolus injected intravenously and images acquired after a stabilization
112 period of 10 min. Doses used for other dyes were: tetramethylrhodamine methyl ester
113 (TMRM, 0.4 mg/kg bw), Dextran Alexa 647 10,000 MW (3 mg/kg bw) and SiR-Actin (7
114 mg/kg bw, Spirochrome AG, Switzerland). GCaMP6s and Hoechst 33342 signals were co-
115 imaged at 900 nm, while GCaMP6s and TMRM were co-imaged at 950 nm. Dextran Alexa
116 647 was excited at 1100 nm or 1180 nm, while SiR-Actin was imaged at 850 nm. Hoechst
117 was injected for automated analysis and images were acquired at a frame rate of 1 frame per
118 second at a laser power of 4.5-10 mW measured at the sample plane, unless otherwise stated.
119 Fields of view of 625 µm x 625 µm were imaged unless otherwise stated. Candesartan (60
120 µg/kg bw) was injected at a rate of 50 µl/min, in a total volume of 120 µl 0.9 % NaCl.
121 Dapagliflozin (DAPA, 4mg/kg bw) was injected at a rate of 50 µl/min, in a total volume of
122 120 µl 0.9 % NaCl and 1.18 % DMSO. *Cis*-diamminedichloroplatinum (II) (cisplatin, 20
123 mg/kg bw) was given by intraperitoneal injection. Cisplatin treated animals were imaged 48
124 and 72 hours after treatment. The number of cells with sustained high baseline Ca^{2+} levels
125 under Ctrl conditions, 48h and 72h after cisplatin treatment were counted from 300 sec time
126 series from different fields of view (625 µm x 625 µm) and normalized to the correspondent
127 tubular area.

128 *Automated analysis of calcium transients*

129 When necessary lateral drift in time series was stabilized using the MultiStackReg (v.1.46.2)
130 plugin for FIJI (42) or NoRMCorre rigid transformation (33). For MultiStackReg the Hoechst
131 channel was used as a reference stack and translation was used as a transformation model.
132 The transformation matrice was then applied to the other channels (GCaMP6s and auto
133 fluorescence). Due to the low laser power employed and the resulting low signal in the
134 Hoechst channel, integrated projections of at least 100 frames (using SUM Z Projection in
135 FiJi) were used for nuclear segmentation using supervised machine learning using Ilastik

using the pixel classification workflow. For DAPA and cisplatin experiments no marker was used and regions of interest were placed manually around cells from different S1 and S2 tubules. Corresponding fluorescence intensities were extracted using the particle analyzer functionality of FIJI.

The obtained fluorescence intensity data was combined into trajectories and further analyzed and visualized using Mathematica (Wolfram Research, Illinois). For the detection of GCaMP6s fluorescence transients, as a first step, trajectories which only contained baseline/noise signal, were identified using a Ljung-Box test. Reasoned by the good baseline stability of the signals, the relative change in fluorescence $\Delta F/F$ of trajectories passing the Ljung-Box test was calculated using the same fixed signal percentile for all trajectories within a dataset (0.72 to 1.03). In order to reduce noise contributions, a low-pass filter was applied (0.5 to 0.8 Hz). Transients were detected based on a fixed $\Delta F/F$ threshold (0.75 to 1.03). All kinetic analysis is based on the thresholded trajectories. To validate this approach, 3 different threshold parameters were tested and the robustness of the analysis was assessed. 4 independent intravital imaging experiments were used for assessment of kinetics of Ca^{2+} transients. Differences between S1 and S2 cells were evaluated with paired two-tailed Student's *t*-test. Significance was set at $p = 0.05$. Temporal whole tubule cyclical excitation patterns were analyzed by manually segmenting tubules and either plotting the mean tubular GCaMP6s fluorescence intensity or by calculating the mean tubular activation probability based on the identified cellular transients. For each time point activation probability = total active cells / total cells.

Results

Generation and characterization of mice expressing GCaMP6s in the kidney

To image Ca^{2+} signaling *in vivo* we utilized a stable transgenic mouse expressing the highly sensitive reporter GCaMP6s (26), under the control of Cre. These animals were crossed with a generalized Cre line (39), to enable imaging of Ca^{2+} signals in all cortical tubular segments. The animals were observed to grow and behave normally, and histological examination of the kidney was unremarkable, whilst immuno-staining for GFP showed expression in all tubular cell types (Figure S1).

Intracellular spatial patterns of calcium transients in proximal tubules

To investigate the spatial nature of Ca^{2+} signals in the PT we co-imaged GCaMP6s with markers of the actin brush border (SiR Actin) and mitochondria (TMRM). We confirmed the presence of widespread spontaneous slow transients in PT cells typically lasting between 10-30 seconds (Figure 1 A-D and Movie S1). In contrast, no changes in Ca^{2+} were observed in the DCT during this period (Figure 1 A-D), despite clear evidence of GCaMP6s expression in this segment (Figure S1). High resolution imaging of single PT cells revealed that the majority of transients originated in the sub-apical region of cells before spreading towards the basolateral side and back (Figure 1 E, Figure S2 and Movie S2). Ca^{2+} transients were not associated with detectable changes in mitochondrial energization (Figure 1 F-H).

Automated analysis of calcium signals along the proximal tubule

Since Ca^{2+} transients in PTs are relatively slow events, we engineered a heated mounting stage with precise temperature control, which uncouples the kidney from body movements and allowed highly stable continuous imaging of the same field of view for up to 30 minutes. Because our goal was to perform prolonged recordings of Ca^{2+} signals, we first tested different excitation laser doses to check for evidence of photo-induced effects. When imaging

every second at a laser power level of 20 mW (measured at the sample), we observed a clear rise in baseline GCaMP6s signal, which occurred exclusively in one population of PTs, subsequently identified as S2 segments (Figure S3). In contrast, when using a lower power of 10 mW, we no longer observed this effect over a recording period of up to 30 minutes, nor did we detect an increase in frequency of transients with time. These experimental conditions were therefore used for subsequent experiments.

To further investigate the nature of Ca^{2+} signals in an unbiased manner, we devised a protocol whereby cells were co-labeled with the nuclear dye Hoechst. Supervised machine learning (22) was then used to segment individual cells based on this signal for automated analysis (Figure 2). Approximately 600 tubular cells were identified per field of view (600 x 600 μm^2), enabling the construction of large scale kinetic maps that could then be probed to investigate underlying spatio-temporal patterns. By using the Ca^{2+}-independent marker Hoechst we were also able to account for cells where no transients were observed during the recorded period as all tubular cells take up the marker. Validation of the signal detected through automated segmentation was performed by manually selecting regions of interest (ROIs) within the same cell (Figure S4). Frequency and duration of transients was highly comparable using the two different approaches.

Projection of the kinetic results onto the structure of the kidney revealed that the rate of transients was much higher in S1 (1.23 ± 0.12 events min^{-1}) than S2 (0.55 ± 0.10 events min^{-1}) PT cells, which were distinguished by characteristic auto-fluorescence signals (Figure 3A-D). In contrast, there was a trend towards a longer duration of transients in S2 cells (16.85 ± 1.36 versus 14.06 ± 1.33 s in S1 cells), but the intensity was similar in both S1 and S2. To investigate the dynamic range of the GCaMP6s sensor *in vivo* and since ischemia is thought to provoke large rises in Ca^{2+} (41, 44), we recorded changes at the end of experiments when

animals were sacrificed. In response to cessation of circulation, the GCaMP6s signal intensity in PT cells increased abruptly to a significantly higher level than during transients (Figure S5). This strongly suggests that under physiological conditions the intracellular Ca^{2+} concentration is tightly controlled and the sensor is not saturated.

Automated analysis of calcium signals in distal tubular segments

In contrast to the DCT, where transients in individual cells were not observed, spontaneous Ca^{2+} transients were observed in the cortical collecting duct (CCD) (Figure 3E-G). However, the number of cells displaying transients (20.92 ± 5.58 %) was considerably lower than in the PT. Moreover, transients in CCD cells were typically longer and of lower amplitude than in PT cells.

Analysis of calcium signals in whole segments of proximal tubules

To further investigate the nature of axial patterns of Ca^{2+} signals along the PT, we injected animals intravenously with a fluorescently labeled 10 kDa dextran. This was rapidly filtered, and appeared first within the lumen of those segments classified as S1 on the basis of auto-fluorescence, and later in S2, thus confirming their identity (Figure 4A). We observed a striking inverse relationship between the time taken for dextran to appear in the lumen and the mean event rate of Ca^{2+} transients in S1 segments (Figure 4B-C), implying that tubular Ca^{2+} activity in S1 is determined by distance from the glomerulus. This relationship was less clear in S2 due to the number of inactive segments.

Although spontaneous Ca^{2+} transients did not arise from adjacent cells simultaneously, by integrating the signal in whole sections of S1 PT segments we observed that in some animals tubular Ca^{2+} changes (Figure 5A-B), as well as activation probability of cells within the tubule (Movie S3), followed a cyclical pattern. Interestingly, the kinetics of this closely matched previously reported oscillations in tubular pressure due to tubulo-glomerular

feedback (TGF) (18). In addition, in response to selective inhibition of solute transport in upstream S1 segments with the SGLT2 blocker DAPA the activation probability increased in downstream S2 segments (Figure 5C-E). Conversely, when we injected animals with the angiotensin II receptor inhibitor candesartan, which acutely decreases glomerular pressure and GFR, PT lumens collapsed and transients stopped abruptly (Figure S6). Taken together, these findings suggest that tubular Ca^{2+} activity might be influenced by glomerular function and luminal solute delivery *in vivo*, although it is important to note that candesartan could also exert direct effects on tubular Ca^{2+} activity via AT-1 receptors.

Calcium signaling in proximal tubules is altered in acute kidney injury

To investigate how Ca^{2+} signaling is affected in an AKI model of direct relevance to humans we injected mice with cisplatin, which causes mitochondrial toxicity in PTs (6). After 48 hours mitochondria in PTs showed evidence of fragmentation and depolarization, which became more severe after 72 hours (Figure 6A). This was associated with an increasing number of PT cells displaying sustained increases in Ca^{2+} - implying a loss of normal Ca^{2+} homeostasis - which did not appear to propagate to adjacent cells (Figure 6A-C). While imaging such cells over time, we observed that they protruded into the tubular lumen and in some cases showed dramatic shedding of apical cellular contents (Movie S4), leading to accumulation of cellular debris with high Ca^{2+} in the tubular lumens (Movie S5). Remaining PT cells had a flattened appearance and severely impaired uptake of fluorescent dextran (Figure 6A-B). Unfortunately, since damaged PTs cells were morphologically very different we could not reliably identify cells using the Hoechst signal and were thus unable to perform automated detection of cells post cisplatin treatment. Nevertheless, visual inspection of temporal color coded large fields of view and manual analysis of selected cells revealed a striking decrease in the rate of spontaneous Ca^{2+} transients in S1 (Figure 6A-D), consistent with a major change in functional phenotype.

Overall, these *in vivo* findings suggest that normal Ca^{2+} homeostasis is lost in metabolically compromised PTs during AKI, and that changes in intracellular Ca^{2+} are associated with major alterations in cell structure and transport function.

Discussion

We have shown that by leveraging a number of technical advances it is possible to perform high resolution and quantitative imaging of Ca^{2+} signals within single renal epithelial cells in living mice, and to map these insights to whole organ architecture. Moreover, changes in Ca^{2+} activity can be followed in real time in response to physiological interventions or in disease models. Using this approach, we have shown: (1) that different tubular segments exhibit characteristic patterns of Ca^{2+} signals; (2) that the majority of Ca^{2+} transients in PT cells originate in the apical region and then propagate basolaterally; (3) that the frequency of transients in S1 decreases with increasing distance from the glomerulus; (4) that activation probabilities in PTs display cyclical patterns; and (5) that intracellular Ca^{2+} signaling is substantially altered in a model of human AKI. We therefore believe this methodology has much potential for future translational kidney research.

GCaMP6s combines a high Ca^{2+} sensitivity with relatively slow kinetics (8), and is therefore ideally suited for following events that occur over long time scales. We have demonstrated that expression of GCaMP6s in the kidney allows detailed imaging of Ca^{2+} signals at laser powers sufficiently low to avoid photo-induced effects. At higher laser powers, we observed toxicity exclusively in S2 PT segments. This could be explained by a high density of peroxisomes in this region (9), which might be sources of laser induced reactive oxygen species (ROS) production.

The most striking finding from our quantitative analysis was that the frequency of Ca^{2+} transients was much higher in S1 cells, which perform the bulk of solute reabsorption post

glomerular filtration (25). Conversely, approximately 40% of S2 cells did not display any spontaneous activity during recording periods up to 30 minutes. However, activity in S2 segments increased in response to upstream inhibition of solute transport in S1. This further supports the notion that these segments are functionally discrete entities (16), and raises the intriguing question as to whether non-active S2 segments could represent a functional reserve capacity for solute transport. The amplitude of transients was similar along the PT, implying a common intracellular process that is tightly regulated, and suggesting that information conveyed by Ca^{2+} signals *in vivo* is predominantly encoded in the frequency. Of note, this is quite different from *in vitro* cell models, where large and sustained rises in amplitude are often reported (34).

By co-imaging with structural markers we observed that PT Ca^{2+} transients typically originate in the apical region before spreading basolaterally, and therefore provide the potential for cross-talk between the two compartments of the cell, which might be important in optimizing the efficiency of vectorial solute transport (12). In stark contrast to PTs, less spontaneous Ca^{2+} activity occurred in DCT cells. Expression of GCaMP6s in this segment was confirmed by immuno-staining and occasional changes in signal were detected, but these were infrequent and often not observed within a 30 minute recording period. Moreover, they typically happened simultaneously in all visible cells from the segment. A plausible explanation for the lack of transients is that DCT cells express high levels of Ca^{2+} binding proteins (24, 29). Furthermore, since they perform transcellular rather than paracellular Ca^{2+} transport, the regulation of Ca^{2+} and its role as a second messenger are likely to be different in this segment. Ca^{2+} transients were observed in CCD cells, which are thought to be flow sensitive (27, 40), and abnormal flow sensing and Ca^{2+} signaling in this region has long been suspected to be central to the pathogenesis of ciliopathies like polycystic kidney disease (15).

Interestingly, the characteristics of CCD transients were different from the PT, suggesting distinct underlying mechanisms.

We found that Ca^{2+} transients in PT whole segments display a cyclical pattern closely matching that reported previously for luminal pressure changes caused by TGF (18). This phenomenon was more obvious in some animals than others, for reasons that are unclear, but might relate to depth of anesthesia, which can have an effect on renal hemodynamics (2). We also observed that S1 Ca^{2+} activity correlates inversely with distance from the glomerulus and abruptly decreased in response to a reduction in GFR. These findings potentially support previous *in vitro* reports suggesting that Ca^{2+} signaling might play a role in the phenomenon of glomerular-tubular balance (43). However, it is important to note that there might be other explanations for cyclical Ca^{2+} activity in the PT besides TGF. Moreover, in addition to decreasing GFR, candesartan could exert direct confounding effects on tubules. Thus, further studies will be required to elucidate whether intracellular Ca^{2+} mediates tubular responses to changes in glomerular function, and if so, how exactly changes in luminal flow are sensed.

Intravital imaging of genetically encoded Ca^{2+} sensors offers much potential for understanding disease mechanisms in the kidney, including in the glomerulus (3, 7). AKI in humans is associated with significant morbidity and mortality (1), but the cellular pathogenesis *in vivo* remains poorly understood. We observed that ischemia induced an abrupt increase in Ca^{2+} in PTs, consistent with reports from others (41). We also found that in response to cisplatin an increasing number of PT cells displayed sustained rises in Ca^{2+}, and subsequently shed apical material in the tubular lumen. We have previously described this phenomenon in response to ischemia (14), and speculate that high intracellular Ca^{2+} might trigger exocytosis (45). Surviving flattened PT cells maintained Ca^{2+} homeostasis despite severe mitochondrial damage, perhaps due to a temporary switch to anaerobic glycolysis

(23). However, both the frequency of Ca^{2+} transients and amount of solute uptake in these cells were markedly reduced, consistent with a substantial change in function.

Despite the valuable insights given by this study we are aware that there are several limitations to our approach, which could be addressed in future studies. First, the relatively slow kinetics of GCaMP6s mean that very rapid signaling events might be missed. Second, although GCaMP6s was detected in all tubular segments, expression levels might vary. Third, our automated analysis protocol does not capture all cells within a field of view, thus it is likely that it slightly underestimates the actual proportion, due to the inherent weakness of 2D Ca^{2+} imaging. Finally, we could not apply the automated analysis approach to damaged cells in the AKI model; however, this might be less of a problem in other disease models where normal tubular cell structure is better preserved.

In summary, we describe a powerful new tool to quantitatively monitor Ca^{2+} changes at high resolution within cells in different tubular segments *in vivo*. This approach has much potential to further understanding of how single cell behavior is integrated with whole organ structure and function, and how these relationships might change in disease states.

Authors contributions

J.R.M., D.H., and A.M.H. conceived and designed the experiments. J.R.M., M.B. and A.F. performed the experiments. J.R.M. and D.H. analyzed the data. A.M.H. wrote the manuscript with input from all authors.

Acknowledgements

The authors gratefully acknowledge support from Dr Claus Schuh, Dr Eilidh Craigie, The Zurich Centre for Microscopy and Image Analysis, The Zurich Centre for Integrative Human Physiology, Spirochrome for the kind gift of the SiR-probe and the laboratory of Prof. Jan Loffing, Zurich, Switzerland for the kind gift of the NCC antibody.

A.M.H. is supported by The Swiss National Centre for Competence in Research (NCCR) Kidney Control of Homeostasis and by a project grant from the Swiss National Science Foundation. J.R.M. is supported by The Marie Curie International Fellowship Programme on Integrative Kidney Physiology and Pathophysiology (IKPP2 - funded by the European Union's Seventh Framework Programme for research, technological development and demonstration under the grant agreement no 608847). The authors also acknowledge support from The Clinical Research Priority Programs "Molecular Imaging Network Zurich" and "Artificial Intelligence in oncological imaging".

Disclosures

None.

References

1. **Bellomo R**, **Kellum JA**, **Ronco C**. Acute kidney injury. *Lancet* 380 Lancet Publishing Group: 756–766, 2012.

2. **Bidani AK**, **Polichnowski AJ**, **Licea-Vargas H**, **Long J**, **Kliethermes S**, **Williamson GA**, **Griffin KA**. BP fluctuations and the real-time dynamics of renal blood flow responses in conscious rats. *J Am Soc Nephrol* 31: 324–336, 2020.

3. **Binz-Lotter J**, **Jüngst C**, **Rinschen MM**, **Koehler S**, **Zentis P**, **Schauss A**, **Schermer B**, **Benzing T**, **Hackl MJ**. Injured podocytes are sensitized to angiotensin II–induced calcium signaling. *J Am Soc Nephrol* 31: 532–542, 2020.

4. **Bootman MD**, **Collins TJ**, **Peppiatt CM**, **Prothero LS**, **MacKenzie L**, **De Smet P**, **Travers M**, **Tovey SC**, **Seo JT**, **Berridge MJ**, **Ciccolini F**, **Lipp P**. Calcium signalling--an overview. *Semin Cell Dev Biol* 12: 3–10, 2001.

5. **Bozic M**, **Valdivielso JM**. Calcium signaling in renal tubular cells. *Adv Exp Med Biol*

740: 933–944, 2012.

6. **Brooks C**, **Wei Q**, **Cho SG**, **Dong Z**. Regulation of mitochondrial dynamics in acute kidney injury in cell culture and rodent models. *J Clin Invest* 119: 1275–1285, 2009.

7. **Burford JL**, **Villanueva K**, **Lam L**, **Riquier-Brison A**, **Hackl MJ**, **Pippin J**, **Shankland SJ**, **Peti-Peterdi J**. Intravital imaging of podocyte calcium in glomerular injury and disease. *J Clin Invest* 124: 2050–2058, 2014.

8. **Chen TW**, **Wardill TJ**, **Sun Y**, **Pulver SR**, **Renninger SL**, **Baohan A**, **Schreiter ER**, **Kerr RA**, **Orger MB**, **Jayaraman V**, **Looger LL**, **Svoboda K**, **Kim DS**. Ultrasensitive fluorescent proteins for imaging neuronal activity. *Nature* 499: 295–300, 2013.

9. **Christensen EI**, **Wagner CA**, **Kaissling B**. Uriniferous tubule: Structural and functional organization. *Compr Physiol* 2: 805–861, 2012.

10. **Dong Z**, **Saikumar P**, **Weinberg JM**, **Venkatachalam MA**. CALCIUM IN CELL INJURY AND DEATH. *Annu Rev Pathol Mech Dis* 1: 405–434, 2006.

11. **Du Z**, **Weinbaum S**, **Weinstein M**, **Wang T**. Regulation of glomerulotubular balance. III. Implication of cytosolic calcium in flow-dependent proximal tubule transport. *Am J Physiol - Ren Physiol* 308: 839–847, 2015.

12. **Duan Y**, **Weinstein AM**, **Weinbaum S**, **Wang T**. Shear stress-induced changes of membrane transporter localization and expression in mouse proximal tubule cells. *Proc Natl Acad Sci U S A* 107: 21860–21865, 2010.

13. **Gailly P**, **Szutkowska M**, **Olinger E**, **Debaix H**, **Seghers F**, **Janas S**, **Vallon V**, **Devuyst O**. P2Y2 receptor activation inhibits the expression of the sodium-chloride

cotransporter NCC in distal convoluted tubule cells. *Pflugers Arch* 466: 2035–47, 2014.

14. **Hall AM**, **Crawford C**, **Unwin RJ**, **Duchen MR**, **Peppiatt-Wildman CM**. Multiphoton imaging of the functioning kidney. *J Am Soc Nephrol* 22: 1297–304, 2011.

15. **Harris PC**, **Torres VE**. Genetic mechanisms and signaling pathways in autosomal dominant polycystic kidney disease. *J. Clin. Invest.* 124 American Society for Clinical Investigation: 2315–2324, 2014.

16. **Hato T**, **Winfree S**, **Day R**, **Sandoval RM**, **Molitoris BA**, **Yoder MC**, **Wiggins RC**, **Zheng Y**, **Dunn KW**, **Dagher PC**. Two-Photon Intravital Fluorescence Lifetime Imaging of the Kidney Reveals Cell-Type Specific Metabolic Signatures. *J Am Soc Nephrol* 28: 2420–2430, 2017.

17. **Healy V**, **Thompson C**, **Johns EJ**. The adrenergic regulation of proximal tubular Na+/H+ exchanger 3 in the rat. *Acta Physiol* 210: 678–689, 2014.

18. **Holstein-Rathlou NH**, **Marsh DJ**. Oscillations of tubular pressure, flow, and distal chloride concentration in rats. *Am J Physiol* 256: F1007-14, 1989.

19. **Jensen MEJ**, **Odgaard E**, **Christensen MH**, **Praetorius HA**, **Leipziger J**. Flow-induced [Ca2+]i increase depends on nucleotide release and subsequent purinergic signaling in the intact nephron. *J Am Soc Nephrol* 18: 2062–70, 2007.

20. **Jobsis PD**, **Rothstein EC**, **Balaban RS**. Limited utility of acetoxymethyl (AM)-based intracellular delivery systems, in vivo: interference by extracellular esterases. *J Microsc* 226: 74–81, 2007.

21. **Komlosi P**, **Banizs B**, **Fintha A**, **Steele S**, **Zhang Z-R**, **Bell PD**. Oscillating cortical thick ascending limb cells at the juxtaglomerular apparatus. *J Am Soc Nephrol* 19: 1940–6, 2008.

22. **Kreshuk A**, **Straehle CN**, **Sommer C**, **Koethe U**, **Cantoni M**, **Knott G**, **Hamprecht FA**. Automated detection and segmentation of synaptic contacts in nearly isotropic serial electron microscopy images. *PLoS One* 6: e24899, 2011.

23. **Lan R**, **Geng H**, **Singha PK**, **Saikumar P**, **Bottinger EP**, **Weinberg JM**, **Venkatachalam MA**. Mitochondrial pathology and glycolytic shift during proximal tubule atrophy after ischemic AKI. *J Am Soc Nephrol* 27: 3356–3367, 2016.

24. **Lee C-T**, **Ng H-Y**, **Lee Y-T**, **Lai L-W**, **Lien Y-HH**. The role of calbindin-D28k on renal calcium and magnesium handling during treatment with loop and thiazide diuretics. *Am J Physiol Renal Physiol* 310: F230-6, 2016.

25. **Maddox DA**, **Gennari JF**. The early proximal tubule: A high-capacity delivery-responsive reabsorptive site. *Am. J. Physiol. - Ren. Fluid Electrolyte Physiol.* 252: 1987.

26. **Madisen L**, **Garner AR**, **Shimaoka D**, **Chuong AS**, **Klapoetke NC**, **Li L**, **van der Bourg A**, **Niino Y**, **Egolf L**, **Monetti C**, **Gu H**, **Mills M**, **Cheng A**, **Tasic B**, **Nguyen TN**, **Sunkin SM**, **Benucci A**, **Nagy A**, **Miyawaki A**, **Helmchen F**, **Empson RM**, **Knöpfel T**, **Boyden ES**, **Reid RC**, **Carandini M**, **Zeng H**. Transgenic mice for intersectional targeting of neural sensors and effectors with high specificity and performance. *Neuron* 85: 942–58, 2015.

27. **Mamenko M V**, **Boukelmoune N**, **Tomilin VN**, **Zaika OL**, **Jensen VB**, **O'Neil RG**, **Pochynyuk OM**. The renal TRPV4 channel is essential for adaptation to increased

dietary potassium. *Kidney Int* 91: 1398–1409, 2017.

28. **Mayrhofer JM**, **Haiss F**, **Haenni D**, **Weber S**, **Zuend M**, **Barrett MJP**, **Ferrari KD**, **Maechler P**, **Saab AS**, **Stobart JL**, **Wyss MT**, **Johannssen H**, **Osswald H**, **Palmer LM**, **Revol V**, **Schuh C-D**, **Urban C**, **Hall A**, **Larkum ME**, **Rutz-Innerhofer E**, **Zeilhofer HU**, **Ziegler U**, **Weber B**. Design and performance of an ultra-flexible two-photon microscope for in vivo research. *Biomed Opt Express* 6: 4228, 2015.

29. **Olinger E**, **Schwaller B**, **Loffing J**, **Gailly P**, **Devuyst O**. Parvalbumin: calcium and magnesium buffering in the distal nephron. *Nephrol Dial Transplant* 27: 3988–94, 2012.

30. **Petersen OH**, **Michalak M**, **Verkhratsky A**. Calcium signalling: Past, present and future. *Cell Calcium* 38: 161–169, 2005.

31. **Peti-Peterdi J**, **Kidokoro K**, **Riquier-Brison A**. Novel in vivo techniques to visualize kidney anatomy and function. *Kidney Int.* 88 Nature Publishing Group: 44–51, 2015.

32. **Peti-Peterdi J**, **Toma I**, **Sipos A**, **Vargas SL**. Multiphoton imaging of renal regulatory mechanisms. *Physiology* 24: 88–96, 2009.

33. **Pnevmatikakis EA**, **Giovannucci A**. NoRMCorre: An online algorithm for piecewise rigid motion correction of calcium imaging data. *J Neurosci Methods* 291: 83–94, 2017.

34. **Raghavan V**, **Rbaibi Y**, **Pastor-Soler NM**, **Carattino MD**, **Weisz OA**. Shear stress-dependent regulation of apical endocytosis in renal proximal tubule cells mediated by primary cilia. *Proc Natl Acad Sci U S A* 111: 8506–11, 2014.

35. **Revell DZ**, **Yoder BK**. Intravital visualization of the primary cilium, tubule flow, and

innate immune cells in the kidney utilizing an abdominal window imaging approach. In: *Methods in Cell Biology*. Academic Press Inc., 2019, p. 67–83.

36. **Riquier-Brison ADM**, **Leong PKK**, **Pihakaski-Maunsbach K**, **McDonough AA**. Angiotensin II stimulates trafficking of NHE3, NaPi2, and associated proteins into the proximal tubule microvilli. *Am J Physiol Renal Physiol* 298: F177-86, 2010.

37. **Schindelin J**, **Arganda-Carreras I**, **Frise E**, **Kaynig V**, **Longair M**, **Pietzsch T**, **Preibisch S**, **Rueden C**, **Saalfeld S**, **Schmid B**, **Tinevez JY**, **White DJ**, **Hartenstein V**, **Eliceiri K**, **Tomancak P**, **Cardona A**. Fiji: An open-source platform for biological-image analysis. *Nat. Methods* 9: 676–682, 2012.

38. **Schuh CD**, **Haenni D**, **Craigie E**, **Ziegler U**, **Weber B**, **Devuyst O**, **Hall AM**. Long wavelength multiphoton excitation is advantageous for intravital kidney imaging. *Kidney Int* 89: 712–9, 2016.

39. **Schwenk F**, **Baron U**, **Rajewsky K**. A cre-transgenic mouse strain for the ubiquitous deletion of loxP-flanked gene segments including deletion in germ cells. *Nucleic Acids Res* 23: 5080–5081, 1995.

40. **Svenningsen P**, **Burford JL**, **Peti-Peterdi J**. ATP releasing connexin 30 hemichannels mediate flow-induced calcium signaling in the collecting duct. *Front Physiol* 4: 292, 2013.

41. **Szebényi K**, **Füredi A**, **Kolacsek O**, **Csohány R**, **Prókai Á**, **Kis-Petik K**, **Szabó A**, **Bősze Z**, **Bender B**, **Tóvári J**, **Enyedi Á**, **Orbán TI**, **Apáti Á**, **Sarkadi B**. Visualization of Calcium Dynamics in Kidney Proximal Tubules. *J Am Soc Nephrol* 26: 2731–40, 2015.

42. **Thévenaz P**, **Ruttimann UE**, **Unser M**. A pyramid approach to subpixel registration

based on intensity. *IEEE Trans Image Process* 7: 27–41, 1998.

43. **Wang T**, **Weinbaum S**, **Weinstein AM**. Regulation of glomerulotubular balance: flow-activated proximal tubule function. *Pflugers Arch. Eur. J. Physiol.* 469 Springer Verlag: 643–654, 2017.

44. **Weinberg JM**, **Davis JA**, **Venkatachalam MA**. Cytosolic-free calcium increases to greater than 100 micromolar in ATP- depleted proximal tubules. *J Clin Invest* 100: 713–722, 1997.

45. **Xu J**, **Toops KA**, **Diaz F**, **Carvajal-Gonzalez JM**, **Gravotta D**, **Mazzoni F**, **Schreiner R**, **Rodriguez-Boulan E**, **Lakkaraju A**. Mechanism of polarized lysosome exocytosis in epithelial cells. *J Cell Sci* 125: 5937–43, 2012.

Figure legends

Figure 1. Spontaneous calcium transients in kidney proximal tubules. (A) Proximal tubule (PT) cells in GCaMP6s mice exhibit spontaneous Ca^{2+} transients under resting conditions, while no changes are observed in the distal tubule (DT). **(B)** Temporal color coded image showing GCaMP6s fluorescence intensity changes in PT cells, but not in a neighboring DT, during a period of 54 sec. **(C-D)** High-resolution temporal color coded image and individual cell traces showing that Ca^{2+} transients do not arise simultaneously in neighboring PT cells. **(E)** Ca^{2+} transients arise in the apical region of PT cells (arrow), then propagate towards the basolateral side. **(F)** TMRM injection enables co-imaging of intracellular Ca^{2+} dynamics and mitochondrial function in PT cells. **(G)** Temporal color coded images of GCaMP6s and TMRM signals over a period of 54 sec. Representative of 3 independent experiments. **(H)** Original GCaMP6s and TMRM fluorescence intensity traces from a single a PT cell. Scale bars, 20 µm in **(A)** and **(E)**, 50 µm in **(B-C)** and **(F-G)**.

Figure 2. Automated analysis workflow of calcium transients in kidney tubular cells. (A) Mice were intravenously injected with the DNA binding dye Hoechst to allow visualization of nuclei from individual tubular cells. Multichannel stacks containing both nuclear and GCaMP6s channels were stabilized using the MultiStackReg plugin for FIJI, and integrated projections of at least 100 frames were used for segmentation of the Hoechst channel. **(B)** Supervised machine learning was used to segment the nuclei and create a mask that enabled **(C)** localization and **(D)** extraction of corresponding intensity changes in the GCaMP6s fluorescence channel (green trace in F). **(E-F)** Computational analysis allowed automated and unbiased detection of Ca^{2+} transients (red and black traces in F). **(G)** Regions of interest (in yellow) were manually drawn for each tubular segment and cells were grouped according to their localization. **(H)** Color coded plot illustrating the percentage of cells with

transients within each segment. Segments with less than 3 cells localized are shown in white and were excluded from further analysis. Scale bar, 50 μm.

Figure 3. Quantitative analysis of calcium transients in kidney proximal tubules. (A) Automated computational analysis of Ca^{2+} signaling in proximal tubule (PT) cells from GCaMP6s mice reveals markedly different baseline kinetics in S1 and S2 segments. Transients are faster and shorter in S1 compared to S2. S1 segments can be differentiated by a vesicular autofluorescence (AF) profile that is absent in S2 segments (AF panel). Color coded kinetic plots displays the event rate of individual cells (GCaMP6s panel) as well as the mean event rate for the segments (right panel). Segments with less than 3 cells with detected transients are shown in white and were excluded from the mean segment event rate analysis. **(B)** Event rate, mean duration and mean fluorescence intensity distributions of Ca^{2+} transients for S1 and S2 tubules from A. **(C)** Original traces from S1 and S2 cells, in orange and blue, respectively. Traces in gray represent the Hoechst fluorescence intensity, which was used for cell localization and tracking. **(D)** Comparison of different parameters of Ca^{2+} transients from S1 and S2 cells assessed from 4 independent experiments for a maximum acquisition time of 900s at a rate of 1 frame per second. SEM - standard error of the mean, * represents $p <= 0.05$ while *** $p <= 0.001$ after two-tailed paired t-test. **(E)** Ca^{2+} transients were also observed in cells in the cortical collecting duct (CCD), but in fewer cells than in the PT. **(F)** Original traces from a CCD cell. Trace in gray represents the Hoechst fluorescence intensity, which was used for cell localization. **(G)** Ca^{2+} transients in CCD cells are longer than in the PT, but show a lower amplitude. Scale bars, 50 μm**.**

Figure 4. Confirmation of proximal tubular segment identity. S1 (highlighted by orange line) and S2 segments were identified based on their auto-fluorescence profiles. **(A)** This manual classification was confirmed by monitoring the appearance of injected fluorescently labeled Dextran 10kDa in the tubular lumen. The fluorescence signal first appears in the

lumens of S1 and later in S2 segments. **(B)** Cells from S1 segments display Ca^{2+} transients more frequently than cells from S2 segments. **(C)** Fluorescence intensity in individual S1 (orange) and S2 (blue) segments after injection of fluorescently labeled Dextran 10kDa (marked by the gray line). Mean is represented by the dashed red line. Representative of 4 independent experiments. Scale bar, 50 µm.

Figure 5. Analysis of calcium signals in whole segments of proximal tubules. (A-B) Integrated intensity image of GCaMP6s fluorescence signal (200 frames). Regions of interest (ROIs) were drawn around 4 individual S1 proximal tubular segments, and the mean signal within each ROI shows a cyclical change over time, closely matching the kinetics of previous reports of oscillations in luminal flow/pressure due to tubulo-glomerular feedback. **(C)** Temporal color coded projections of GCaMP6s signal in the kidney, showing baseline Ca^{2+} transients in S2 proximal tubule (PT) cells within 400 sec. Upon intravenous injection of DAPA (4 mg/kg bw) rate of transients increases in S2 PT tubules. **(D)** Event rate was calculated from 3 independent experiments, from a total of 9 S1 tubules (155 cells) and 10 S2 tubules (161 cells). Baseline event rate calculation was performed from 0 to 400 sec, while for DAPA 1201 to 1600 sec were analyzed. **(E)** Individual cells were grouped per tubule type and activation probability for S1 and S2 tubular segments calculated for 3 independent experiments (each trace represents a different experiment, and activation probability = total active cells / total cells). * represents $p <= 0.05$ after two-tailed paired t-test. Scale bars, 50 µm.

Figure 6. Calcium signaling is altered in proximal tubules in cisplatin induced acute kidney injury. (A) GCaMP6s male mice were either vehicle injected (Ctrl, 0.9 % NaCl) or treated with cisplatin (20 mg/kg). Animals were imaged 48h and 72h after injection. Mitochondria in proximal tubules (PTs) loaded with TMRM are damaged and depolarized, and by temporal color coding the frequency of Ca^{2+} transients is reduced in cisplatin treated

571 animals comparatively to vehicle treated animals. A number of cells (red circles) display
572 sustained high Ca^{2+} levels throughout the imaging period. Dextran is still filtered, but uptake
573 into PT cells is markedly reduced after 48h and more dramatically after 72h of cisplatin
574 treatment. Representative images of 3 (Ctrl), 2 (48h cisplatin) and 4 (72h cisplatin)
575 independent experiments. **(B)** Higher magnification images reveal flattened cells,
576 fragmentation of mitochondria (TMRM) and cellular debris in tubular lumens (arrow). A
577 single PT cell (red circle) can be observed with a sustained high Ca^{2+} level, but this does not
578 propagate to the surrounding cells. **(C)** Number of cells with high baseline Ca^{2+} levels under
579 Ctrl conditions, 48h and 72h after cisplatin treatment per mm^2 of tubular surface. Different
580 fields of view are plotted from 3 (Ctrl), 2 (48h cisplatin) and 4 (72h cisplatin) independent
581 experiments from a total of 220, 190 and 187 tubules, respectively. * represents p<= 0.05,
582 while ** p<=0.01 compared to the Ctrl group after one way ANOVA. (**D**) Event rate was
583 calculated from 4 (Ctrl) and 3 (72h cisplatin) independent experiments, from a total of 388
584 and 482 S1 cells, respectively. Baseline event rate calculation was performed from 0 to 400
585 sec. * represents p<= 0.05, while ** p<=0.01 after two-tailed unpaired t-test. Scale bars, 50
586 µm.

587

Figure 1

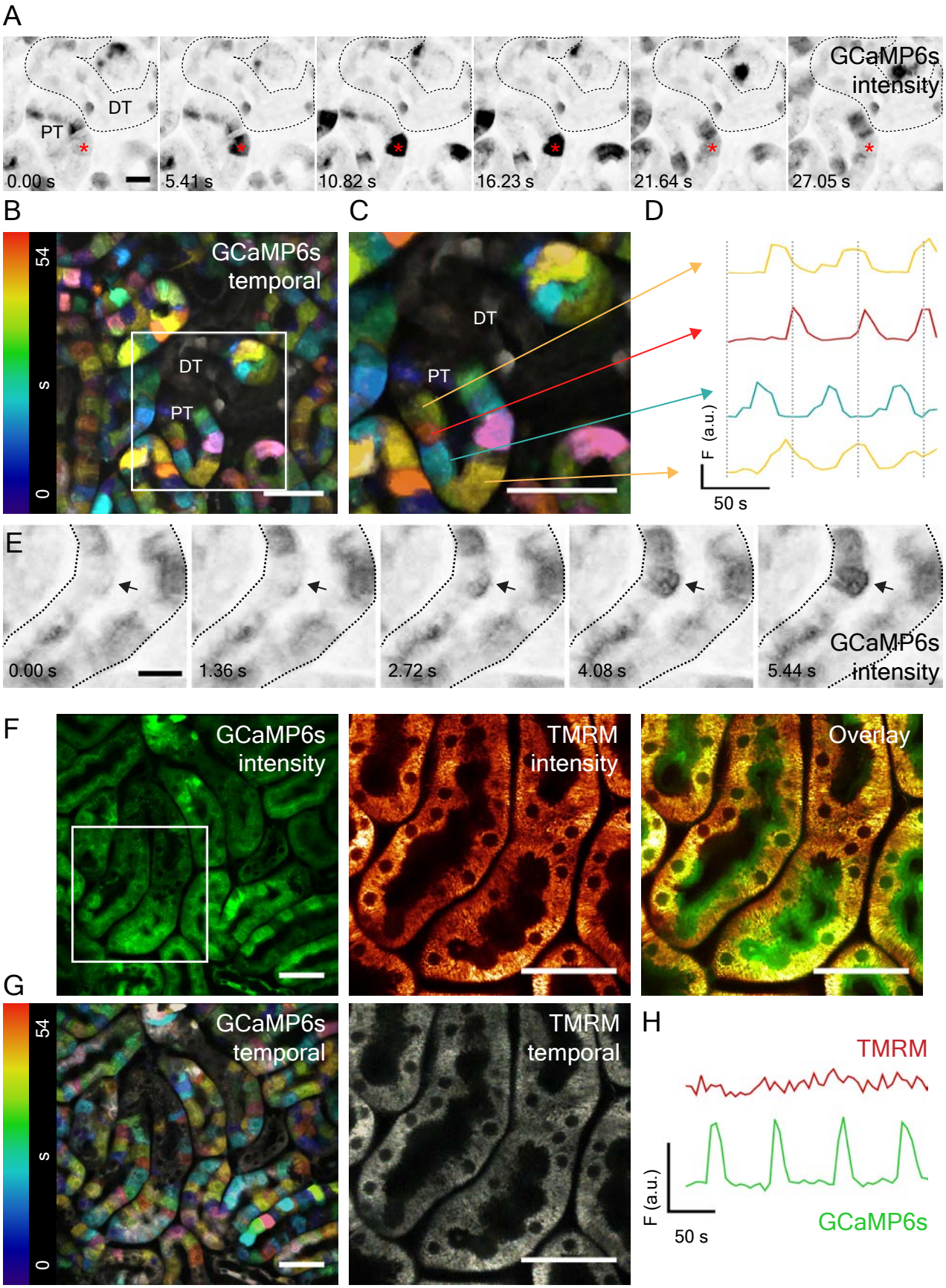
A
DT
PT
0.00 s
5.41 s
10.82 s
16.23 s
21.64 s
27.05 s
GCaMP6s intensity
B
GCaMP6s temporal
54
s
0
DT
PT
C
DT
PT
D
F (a.u.)
50 s
E
0.00 s
1.36 s
2.72 s
4.08 s
5.44 s
GCaMP6s intensity
F
GCaMP6s intensity
TMRM intensity
Overlay
G
GCaMP6s temporal
TMRM temporal
54
s
0
H
TMRM
F (a.u.)
50 s
GCaMP6s

Figure 2

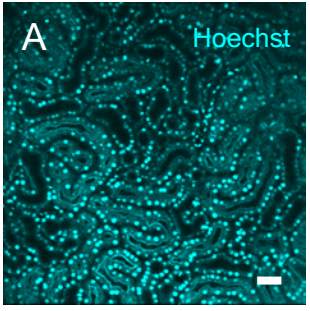
A
Hoechst

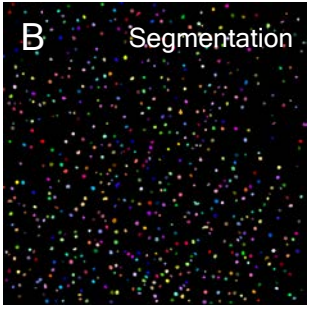
B
Segmentation

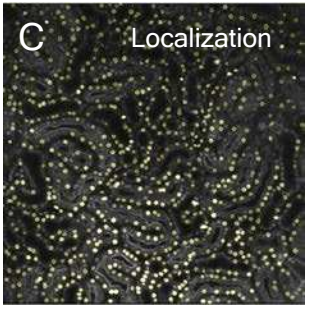
C
Localization

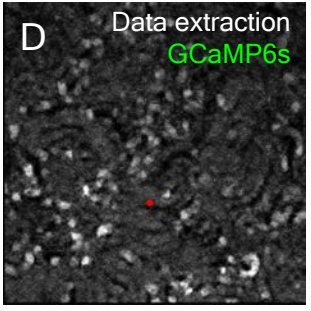
D
Data extraction
GCaMP6s

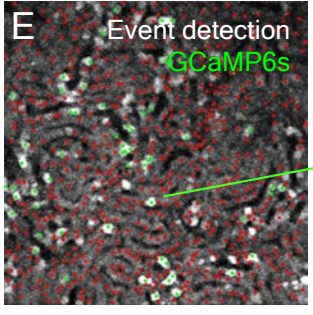
E
Event detection
GCaMP6s

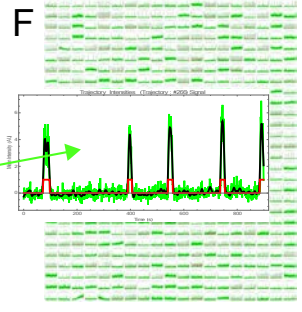
F

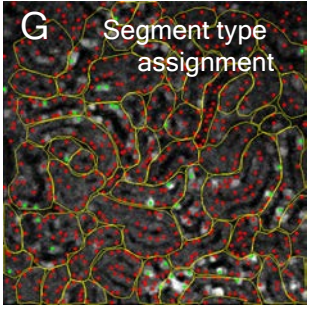
G
Segment type
assignment

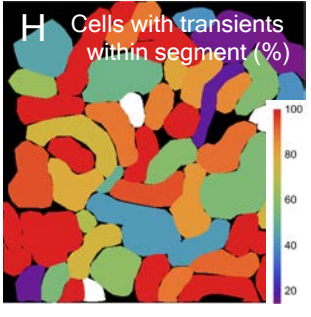
H
Cells with transients
within segment (%)
100
80
60
40
20

Figure 3

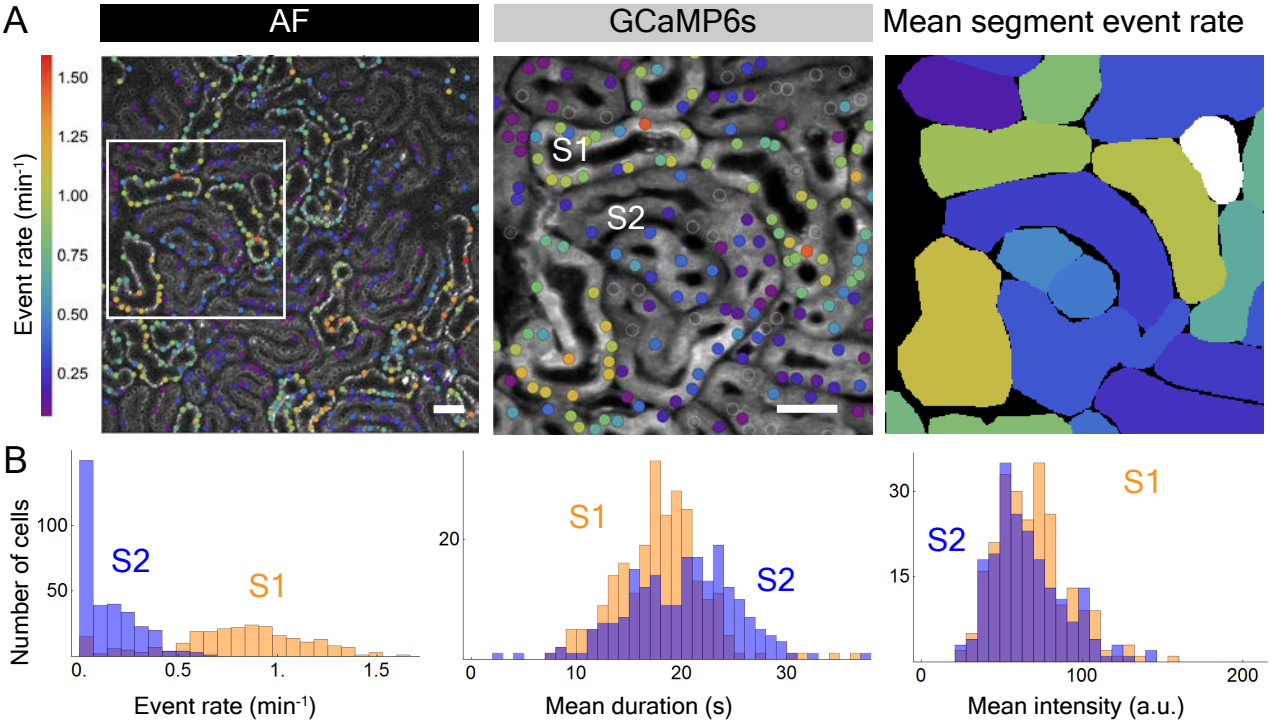

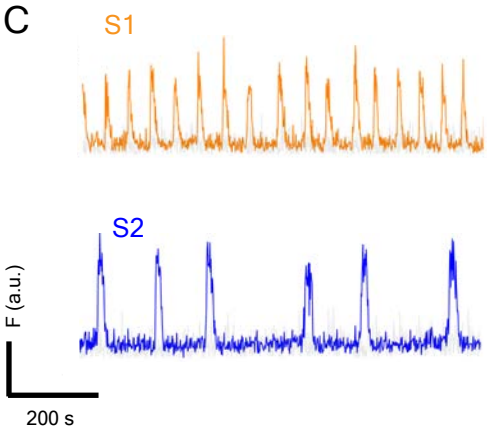

D

Parameter	S1 Mean	S1 SEM	S2 Mean	S2 SEM	p value	
% Cells with detected transients within segments	87.83	2.65	60.25	5.36	0.0101	*
Event rate (min^{-1})	1.23	0.12	0.55	0.10	0.0003	***
Mean duration (s)	14.06	1.33	16.85	1.36	0.08442	
Delta F/F0 (a.u.)	1.81	0.14	1.73	0.12	0.64858	
% Segments without detected transients	0.00	0.00	6.01	3.90	0.27405	
Total Cells	1005		1040			
Total Segments	104		101			
Number of animals	4		4			

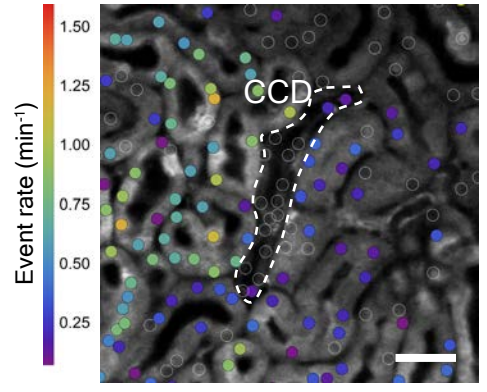

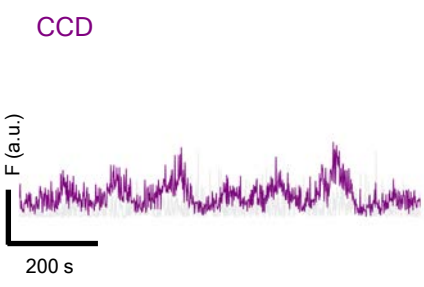

G

Parameter	CCD Mean	CCD SEM
% Cells with detected transients within segments	20.92	5.58
Event rate (min^{-1})	0.81	0.35
Mean duration (s)	27.08	15.04
Delta F/F0 (a.u.)	1.17	0.03
% Segments without detected transients	20.63	8.50
Total Cells	105	
Total Segments	16	
Number of animals	4	

Figure 4

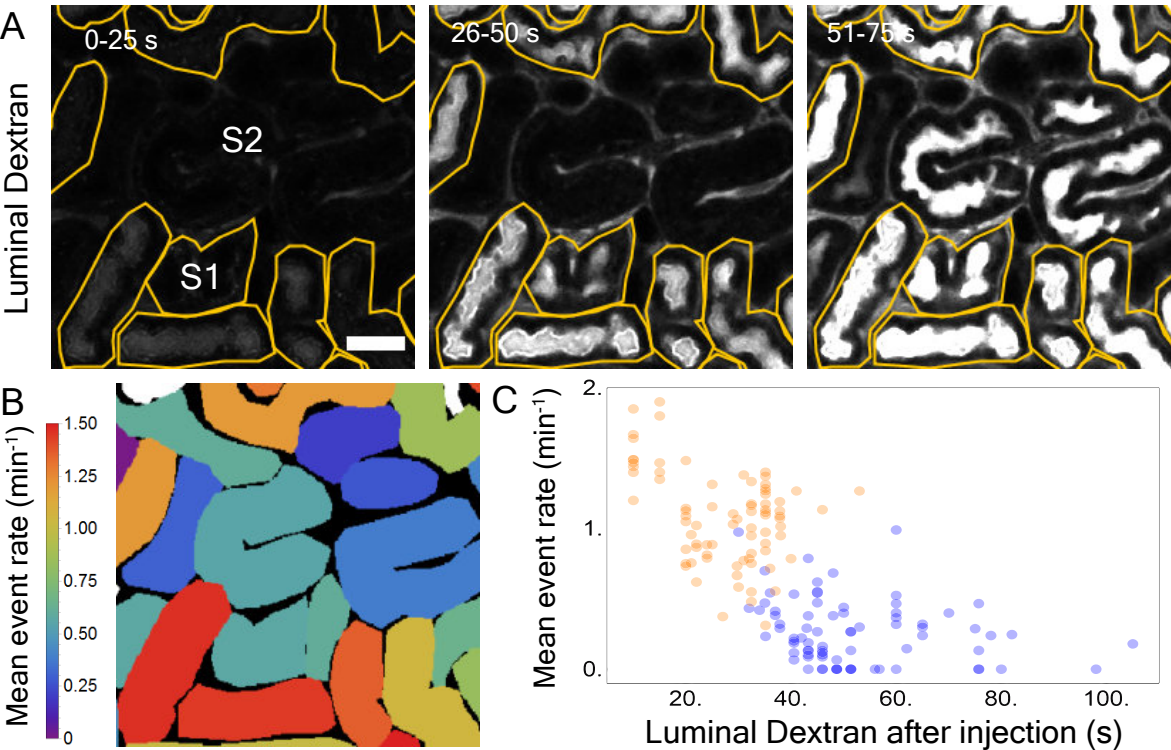
A
Luminal Dextran
0-25 s
26-50 s
51-75 s
S2
S1
B
Mean event rate (min-1)
1.50
1.25
1.00
0.75
0.50
0.25
0
C
Mean event rate (min-1)
2.
1.
0.
20.
40.
60.
80.
100.
Luminal Dextran after injection (s)

Figure 5

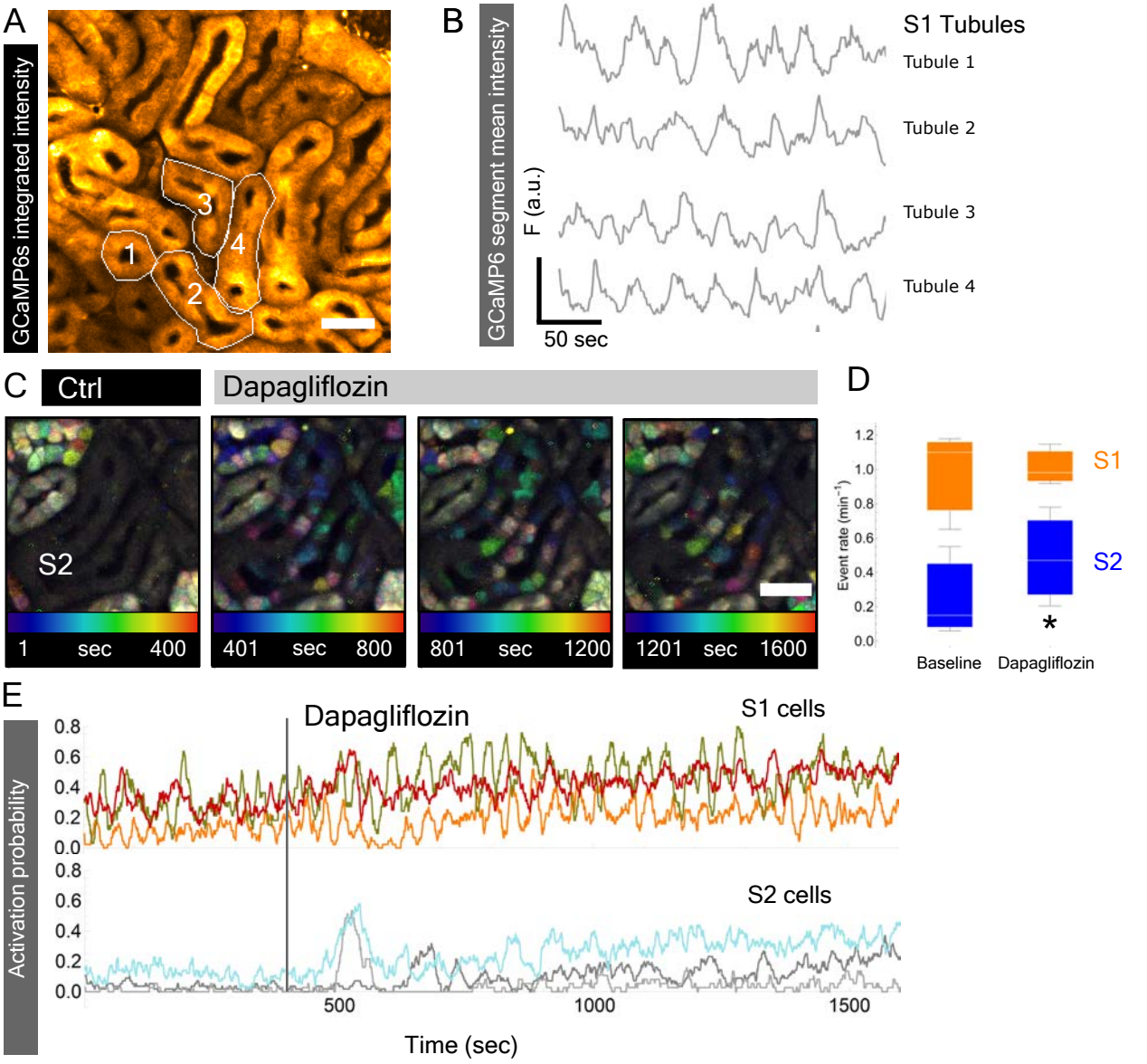
A
GCaMP6s integrated intensity
1
2
3
4
B
GCaMP6 segment mean intensity
F (a.u.)
50 sec
S1 Tubules
Tubule 1
Tubule 2
Tubule 3
Tubule 4
C
Ctrl
Dapagliflozin
S2
1 sec 400
401 sec 800
801 sec 1200
1201 sec 1600
D
Event rate (min⁻¹)
1.2
1.0
0.8
0.6
0.4
0.2
0.0
S1
S2
*
Baseline
Dapagliflozin
E
Activation probability
Dapagliflozin
S1 cells
S2 cells
0.8
0.6
0.4
0.2
0.0
500
1000
1500
Time (sec)

Figure 6

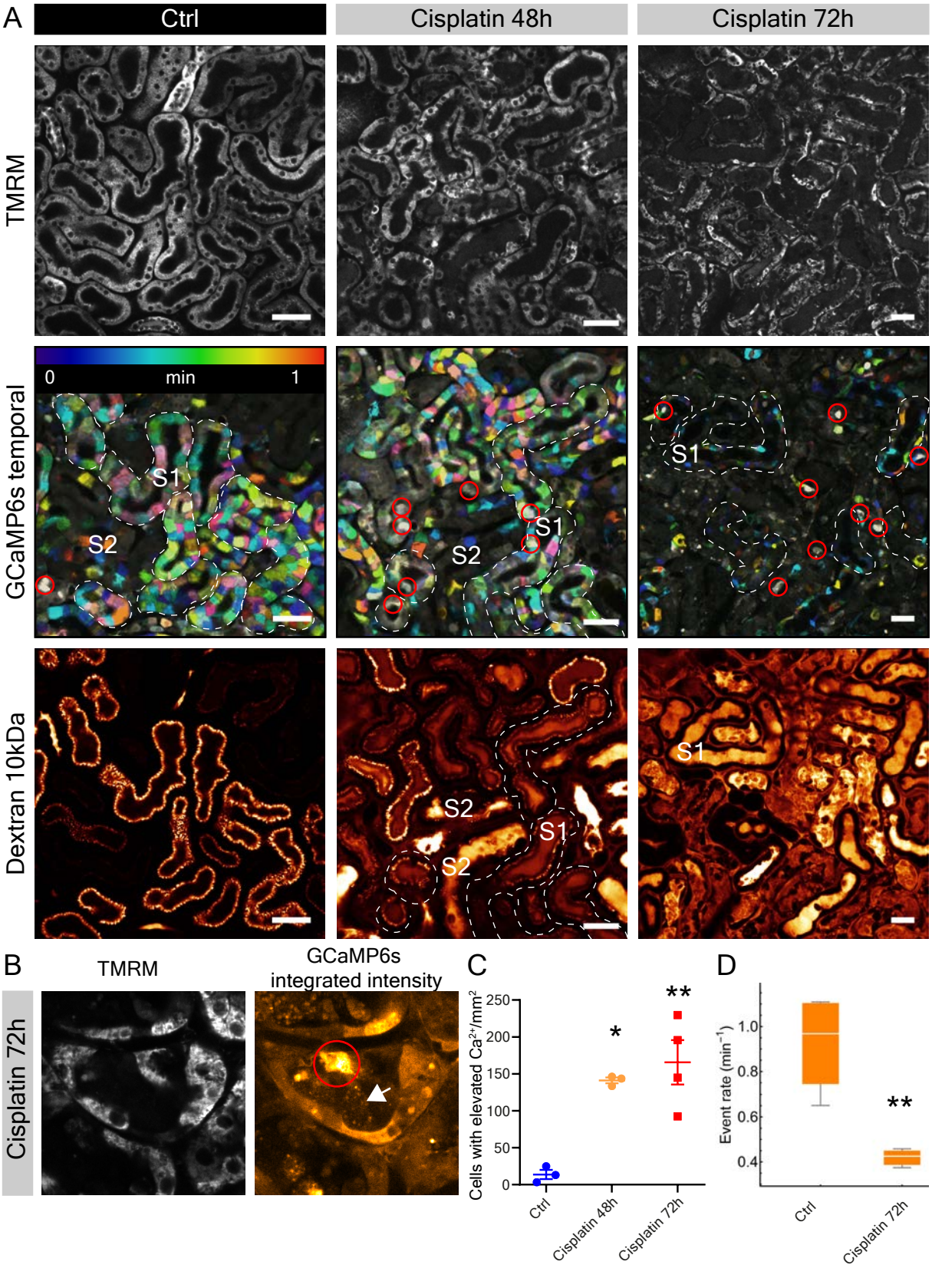
A
Ctrl
Cisplatin 48h
Cisplatin 72h
TMRM
GCaMP6s temporal
0
min
1
S1
S2
S1
S2
S1
Dextran 10kDa
S2
S1
S2
S1
B
TMRM
GCaMP6s
integrated intensity
Cisplatin 72h
C
Cells with elevated Ca2+/mm2
250
200
150
100
50
0
*
**
Ctrl
Cisplatin 48h
Cisplatin 72h
D
Event rate (min-1)
1.0
0.8
0.6
0.4
**
Ctrl
Cisplatin 72h